MNRAS **000**, 1–11 (2021) Preprint 11 June 2021 Compiled using MNRAS LaTeX style file v3.0

Planet Hunters TESS IV: A massive, compact hierarchical triple star system TIC 470710327

N. L. Eisner[1,2]★, C. Johnston[2,3], S. Toonen[4], A. J. Frost[2], C. Lintott[1], S. Aigrain[1], S. Jassens[2], H. Sana[2], D. Fabrycky[5], M. Abdul-Masih[6,2], P. Beck[7], E. Bordier[6,2], D. Bollen[2], E. Cannon[2], A. Escorza-Santos[6,2], M. Fabry[2], L. Hermansson[8], S. Howell[9], S. Sheyte[2], PHT citizen scientists et al.[12]

[1]*Sub-department of Astrophysics, University of Oxford, Keble Rd, Oxford, United Kingdom*
[2]*Institute of Astronomy, KU Leuven, Celestijnenlaan 200D, 3001 Leuven, Belgium*
[3]*Department of Astrophysics, IMAPP, Radboud University Nijmegen, P. O. Box 9010, 6500 GL Nijmegen, the Netherlands*
[4]*Anton Pannekoek Institute for Astronomy, University of Amsterdam, 1090 GE Amsterdam, The Netherlands*
[5] *Department of Astronomy and Astrophysics, University of Chicago, 5640 S. Ellis Ave, Chicago, IL 60637, USA*
[6]*European Southern Observatory, Alonso de Córdova 3107, Vitacura, Casilla 19001, Santiago de Chile, Chile*
[7]*Institute of Physics, University of Graz, NAWI Graz, Universittsplatz 5/II, 8010 Graz, Austria*
[8]*Uppsala*
[9]*Gemini Observatory, Northern Operations Center, 670 North A'ohoku Place, Hilo, HI 96720, USA*
[10]*University of Queensland?*
[11]*Sydney Institute for Astronomy (SIfA), School of Physics, The University of Sydney, NSW 2006, Australia*
[12]*Citizen Scientist, Zooniverse c/o University of Oxford,Keble Road, Oxford OX1 3RH, UK*

Accepted XXX. Received YYY; in original form ZZZ

ABSTRACT

We report on the discovery and analysis of a massive, compact, hierarchical triple system (TIC 470710327) initially identified by citizen scientists in data obtained by NASA's Transiting Exoplanet Survey Satellite (*TESS*). Spectroscopic follow-up observations obtained with the HERMES spectrograph, combined with eclipse timing variations (ETVs), confirmed that the system is comprised of three OB stars, with a compact 1.10 d eclipsing binary and a non-eclipsing tertiary on a 52.04 d orbit. Dynamical modelling of the system (radial velocity and ETVs) revealed a rare configuration wherein the the tertiary star (O9.5-B0.5V; 14-17 $M_{\odot}$) is more massive than the combined mass of the inner binary (10.9-13.2 $M_{\odot}$). Given the high mass of the tertiary, we predict that this system will undergo multiple phases of mass transfer in the future, and likely end up as a double neutron star gravitational wave progenitor or an exotic Thorn-Zytkow object. Further observational characterisation of this system promise constraints on both formation scenarios of massive stars as well as exotic evolutionary end-products.

Key words: keyword1 – keyword2 – keyword3

1 INTRODUCTION

Despite their intrinsic rarity as implied by the initial mass function (IMF; see, e.g. Salpeter 1955; Bastian et al. 2010; Dib et al. 2017), massive stars ($M \geq 8$ $M_{\odot}$) provide radiative, dynamical and chemical feedback to their environment, driving evolution on a wide range of scales. The physical processes responsible for the formation, evolution, and death of massive stars, however, are not well understood (e.g., Zinnecker & Yorke 2007; Tan et al. 2014). The study of these processes is further complicated by the multiplicity characteristics of massive stars, i.e., the property that massive stars often have nearby stellar companions (Sana et al. 2012), which can affect their properties and evolution at all stages of their lives.

Large scale spectroscopic, interferometric, and high contrast imaging surveys of OB stars have demonstrated that most, if not all, massive stars are formed in a binary or higher order multiple system (Sana et al. 2013, 2014; Kiminki & Kobulnicky 2012; Aldoretta et al. 2015; Moe & Di Stefano 2017; Maíz Apellániz et al. 2019; Rainot et al. 2020; Bodensteiner et al. 2021). However, due to the high intrinsic brightness of massive stars, detecting and characterising non-eclipsing lower mass close companions using spectroscopy alone is challenging. Detailed characterisation of close companions,

---

★ E-mail: nora.eisner@new.ox.ac.uk

therefore, often relies on the detection of eclipses or other dynamical effects caused by the presence of a close companion, such as radial velocity (RV) or eclipse timing variations (ETVs). Observations of the latter were made possibly with the advent of space-based photometric surveys with long time-base, high-precision, and high-cadence observations such as CoRoT, *Kepler*, *K*2 and the Transiting Exoplanet Survey Satellite (*TESS*). These space-based missions have enabled the detection of dozens of new triple or higher-order multiple systems through ETVs or multiply eclipsing events (Conroy et al. 2014; Marsh et al. 2014; Borkovits et al. 2015; Rappaport et al. 2017; Hajdu et al. 2017; Sriram et al. 2018; Li et al. 2018; Borkovits et al. 2021). Detailed modelling of such systems has revealed absolute masses of the stellar components in some cases, and allowed for the derivation of mass ratios in others, even in the absence of eclipses (Borkovits et al. 2016).

The identification and characterisation of a large sample of massive stars in multiple systems is crucial to discriminate between different formation and evolution scenarios, to place constraints on theoretical models and to understand the interactions and effects of multiple stars. It has already been shown that the complex interactions between tides, angular momentum exchange, and stellar evolution in binary and higher order multiples fundamentally affect the evolution, and thus the end product, of nearly 70% of all O- and B-type stars. In compact binary orbits, for example, processes including mass transfer, exchange of angular momentum and stellar mergers can open up new evolutionary pathways and end-products such as X-ray binaries, γ-ray bursts, stellar mergers, and gravitational wave events (Sana et al. 2012; de Mink et al. 2013).

The addition of a nearby third body further complicates the evolution. Interactions between three stars can induce different evolutionary pathways through von Zeipel-Kozai-Lidov cycles (ZKL; Kozai 1962; Lidov 1962; Naoz 2016; Ito & Ohtsuka 2019), or result in tertiary driven mass transfer that can lead to mergers, exotic common envelope systems, close double or triple degenerate systems, or contribute to the population of walk-away and run-away systems in our galaxy (Antonini et al. 2017; Renzo et al. 2019; Stephan et al. 2019; Leigh et al. 2020a; Hamers et al. 2021; Glanz & Perets 2021).

Further considerations need to be made for triple systems where the inner stellar binary is orbited by a third body with a longer orbital period, known as a hierarchical triple system. Such a configuration often results in measurable dynamical effects. If the orbital periods and the separations involved are short enough, these effects can be studied with a combination of ETVs (caused by light travel time effects and direct third-body perturbations) and/or RV observations. Measurements of both ETVs and RVs allows for the determination of precise stellar mass ratios and orbital parameters, including the mutual inclination between the inner and the outer orbit of the triple, which is thought to be indicative of the formation history.

In this paper we present a new compact, hierarchical triple system identified in *TESS* data consisting of three O- and B-type stars. The system, which shows large ETV and RV variations, contains an inner $\sim$ 1.1 d eclipsing binary and massive O9.5-B0.5V tertiary orbiting a common centre of mass in a $\sim$ 52 d orbit. The discovery of the system and the data are discussed in Sections 2 - 4. Section 5 outlines the analysis of the photometric and spectroscopic data and Section 6 discusses the system configuration, stability, formation and possible future evolution scenarios. Finally, the conclusions are presented in Section 7.

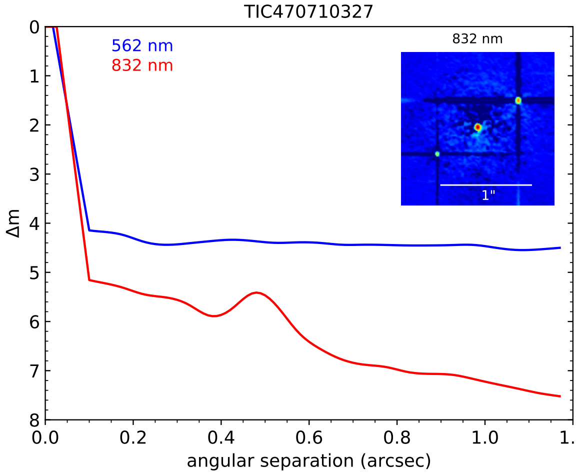

Figure 1. Contrast curves showing the 5 σ detection sensitivity and speckle auto-correlation functions for filters centred on 562 nm (blue) and 832 nm (red).

2 THE TARGET AND ITS SURROUNDINGS

TIC 470710327 (BD+61 2536, TYC 4285-3758-1, V=9.6, parallax = 1.06 mas) was initially identified as an early B-type star by Brodskaya (1953) and as a short period eclipsing binary with a period of 1.1047 d using photometric data obtained with the 0.25-m Takahashi Epsilon telescope in Mayhill, New Mexico, USA (Laur et al. 2017). The target is not a known member of a cluster or OB association (Laur et al. 2017). Two epochs of speckle interferometric measurements revealed a close companion at $\sim$ 0.5", with the position angle and distance of the companion advancing from θ = 306.2 deg and ρ = 0.533" in 1987.7568 (Hartkopf et al. 2000) to θ = 303.7 deg and ρ = 0.502"in 2003.9596 (Hartkopf et al. 2008).

In order to calculate the magnitude differences between TIC 470710327 and the $\sim$ 0.5" companion, hereafter TIC 470710327′, we performed speckle imaging using the Zorro instrument on the 8.1-m Gemini South telescope on Cerro Pachón, Chile (Matson et al. 2019; Howell et al. 2011). Observations were carried out on 15 August 2020 using the two-color diffraction-limited optical imager with 60 msec exposures in sets of 1000 frames. The 5 σ detection sensitivity and the speckle auto-correlation function are shown in Figure 1. The data confirmed that the companion star is located at an angular separation of 0.529" with a position angle of 304.5 deg, which is in agreement with previous observations (Hartkopf et al. 2000, 2008). The data showed that the companion has a magnitude difference of Δm=1.17 mag at 562 nm and of Δm=1.13 mag at 832 nm.

To quantify the light contribution of nearby stars, we queried the early Gaia Data Release 3 catalog (eDR3; Gaia Collaboration et al. 2020). This search revealed a bright (V = 11.6, ΔTmag = 2.4) nearby star at a separation of $\sim$ 22" (LS I +61 72), as well as a further six stars with a $\Delta T_{mag} < 5$ within 100" of the target (listed in Table 1). The light contribution of these stars to our photometric observations will be discussed in Section 3.

Overall, the triple system TIC 470710327 presented in this paper consists of a $P_1 \sim 1.1$ d eclipsing binary with a $P_2 \sim 52$ d non transiting tertiary. Hereafter, the two stars in the inner, short period binary will be referred to as stars A and B, while the tertiary on the wide, outer orbit will be referred to as star C. The 0.5" companion star will be referred to as TIC 470710327′. Using the Gaia eDR3 list of sources in a 2" radius to determine the local field density, and the magnitude contrasts given by the speckle observations, we show that the spurious association probability between TIC 470710327′ and TIC 470710327 is ~ 1×10^{-5}. This means that statistically there is an association between the target and the nearby companion. However, for the remainder of this paper we will assume that TIC 470710327′ has no dynamical effect on the triple system.

3 PHOTOMETRIC DATA AND ETVS

3.1 *TESS*

TIC 470710327 was identified as a potential multiple system by citizen scientists taking part in the Planet Hunters TESS (PHT) citizen science project (Eisner et al. 2020). PHT, which is hosted by the Zooniverse platform (Lintott et al. 2008, 2011), engages nearly 30,000 registered volunteers in the search for planetary transit signals in 2-minute cadence light curves obtained by the the Transiting Exoplanet Survey Satellite (*TESS*, Ricker et al. 2015). In brief, each light curve is seen by 15 volunteers who identify times of transit-like events. Once a volunteer has classified a target, they are able to discuss the target on a discussion forum, and flag interesting systems to the PHT science team using searchable hashtags. TIC 470710327 was flagged as an interesting system on the discussion forum on 6th December 2019 [1], due to the light curve containing multiple periodic signals: P_1 ~ 1.10 d, P_3 ~ 9.97 d and P_4 ~ 4.01 d. We note that for the remainder of this paper we assume that P_3 and P_4 are not dynamically associated with the triple system, as discussed further in Section 6.1.

TIC 470710327 was monitored by *TESS* in the 2-minute cadence data during Sectors 17, 18 and 24 of the nominal mission. The full *TESS* data set, displayed in Fig. 2, spans ~230 days, with the first subset covering nearly 60 days continuously, followed by a large gap of 140 days, before the second ~ 30 day subset of observations. Visual inspection of the full *TESS* light curve (Fig 2) reveals a clear ~1.10 d eclipsing binary system. The presence of eclipses implies an inclination (i_1) close to 90 deg.

The pixel aperture used to extract the light curve, as determined by the *TESS* pipeline at the Science Processing Operations Center (SPOC, Jenkins et al. 2016), is displayed as the red outline in Fig. 3. The orange circles indicate the position of nearby stars that have a *TESS* magnitude difference $<5\Delta T_{\rm mag}$ from the target star, as queried from Gaia eDR3 (Gaia et al. 2018). Considering all sources with a $\Delta T_{\rm mag} < 5$ within 100" of the target (listed in Table 1), we expect TIC 470710327 (including the 0.5" companion, TIC 470710327′) to contribute 88-89.5% of the total light in the *TESS* light curve.

Similarly, using the magnitude contrast derived from by the speckle imaging, we estimate that TIC 470710327′ contributes ~26% of the observed light at 832 nm. Thus, given the ~10.5 - 12% light contribution of the companion at 22", we estimate that TIC 470710327 and TIC 470710327′ contribute ~65% and ~23% of the total light observed by *TESS*, respectively. For the remainder of the paper we assume that the periodic signals P_3 ~ 9.97 d and P_4 ~ 4.01 d, which are not thought to be dynamically associated with the triple system, originate from this composite contaminating light.

Table 1. Nearby GAIA eDR3 sources with within 100" and Δ Tmag < 5 of the target.

2MASS Identifier	Distance (arcsec)	Δ Tmag	Δ Vmag
23491896+6157459	0.000	0.00	0.00
23491667+6158004	21.845	2.40	2.35
23492132+6157124	37.395	4.76	5.75
23492010+6156568	49.643	4.82	5.07
23491426+6157050	52.642	4.38	5.64
23490933+6158367	84.892	4.65	5.36
23493217+6157231	95.863	3.35	3.69
23492162+6159230	98.898	4.45	5.11

3.2 Additional photometric observations

In addition to the *TESS* data, there are 531 archival photometric observations obtained with the 0.25-m Takahashi Epsilon telescope in Mayhill, New Mexico, USA between 2011 and 2013 (Laur et al. 2017) as well as 108 phototometric observations taken over 600 days by the SuperWASP-N camera located on La Palma, Canary Islands (Pollacco et al. 2006). Furthermore, we obtained 456 photometric observations in the [XX] band between 2020 March 21 and March 30, using [ask Lars for details]. Finally, we obtained 1415 photometric observations using the Las Cumbres Observatory (LCO) global network of fully robotic 0.4-m/SBIG and 1.0-m/Sinistro facilities. The LCO data were reduced and calibrated using the standard LCO Banzai pipeline. We performed aperture photometry for TIC 470710327 and 5 comparison stars using the open source SEP package (Barbary 2016; Bertin & Arnouts 1996).

These archival and new photometric measurements significantly increased the baseline of the observations, allowing us to refine the period of the inner binary to P_1=1.104686±0.000004 d. Furthermore, the facilities used to obtain these measurements have significantly smaller pixel scales than *TESS*, such that the extracted light curves do not include TIC 470710327′. This allowed us to confirm the stability of the dominant periodic signal, P_1=1.10 d, and verify that this binary signal does not originate from TIC 470710327′. Due to the sparse sampling of these four data sets we are unable to use these observations to investigate the stability or the origin of either the P_3 nor the P_4 signals.

3.3 Eclipse Timing Variations

Eclipse timing variations (ETVs), which are deviations from strict periodicity in the mid-point of an eclipse or transit event, can be used to detect or study additional gravitating bodies in a system. The variations can be induced by a number of different physical mechanisms, such as mass transfer between stars, or the time-dependent tidal forces of a close tertiary object. We searched for deviations from the predicted linear ephemeris of P_1, given by:

$$T_{\rm min,P/S} = t_{0,P/S} + 1.104686 \times (E),$$

where E is the cycle number since the reference orbit, $t_{0,P}$= 2458766.2700 is the reference epoch for primary eclipses, and $t_{0,S}$ = 2458766.82234 is the reference epoch for secondary eclipses.

Using the *TESS* data only, we determined the deviations from this ephemeris following the methodology outlined by Li et al. (2018). In brief, we determined the eclipse regions of the primary and secondary eclipses by extracting the minima of the second derivative around the time of the eclipses in the phase folded folded light curve. These translate to the phases of ingress and egress.

---

[1] `https://www.zooniverse.org/projects/nora-dot-eisner/planet-hunters-tess/talk/2112/1195850?comment=2011869&page=1`

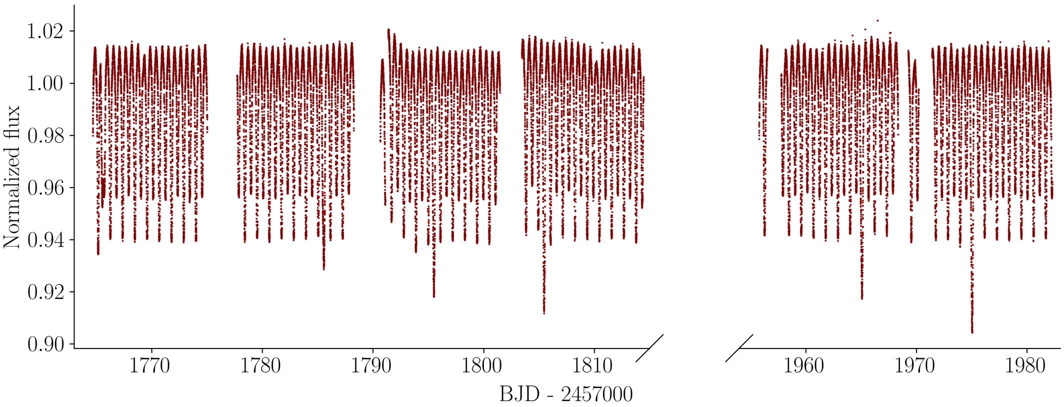

Figure 2. Full *TESS* light curve of TIC 470710327 obtained during sectors 17,18 and 24. The dashed lines on the x-axis show a split in the axis.

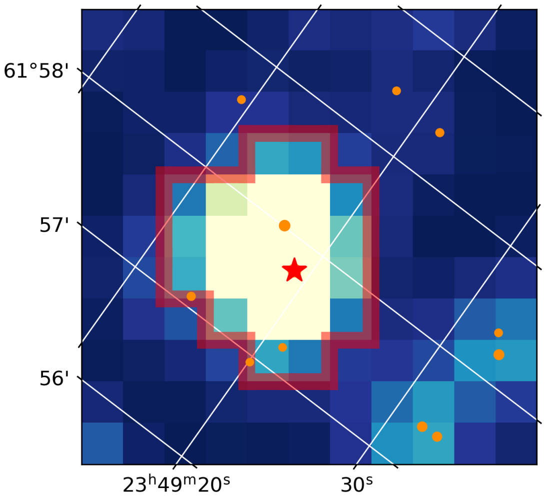

Figure 3. Nearby stars. Red outline shows the *TESS* aperture that as used to extract the flux in Sector 14.

Prior to this we masked the P_3=9.9733 d signal from the light curve. Additional lower amplitude signals were not removed, due to the risk of introducing spurious signals.

Next, we generated a model of the primary eclipse by fitting a trapezoid to the smoothed, phase folded and subsequently binned light curve. This model was then fit to each individual primary transit where the only two free model parameters were the time of eclipse and the slope of an underlying linear trend. The latter was to allow for systematic effects that change the slope of the eclipse. The same methodology was independently carried out for the secondary eclipses. The individual fits to all eclipses, including both the primary and the secondary eclipses of the P_1=1.1047 d signal, were optimised using a Markov chain Monte Carlo (MCMC) approach, using the open source software EXOPLANET (Foreman-Mackey et al. 2021). The observed minus calculated times of eclipse (O-C), which show variations on the range of ∼ ± 6 minutes, are listed in Tables A2 and A3 for the primary and secondary eclipses, respectively. The periodicity in the O-C curves, of P_2 ∼52 d, is also observed in the radial velocities (Section 4), and is thus attributed to the tertiary star of the triple system, as discussed further in Section 5.1.

4 SPECTROSCOPIC OBSERVATIONS AND RADIAL VELOCITY EXTRACTION

We obtained 24 spectra between 31 January and 5 October 2020 using the HERMES spectrograph (R∼85 000, Raskin et al. 2011) on the 1.2-m Mercator telescope at Observatorio del Roque de los Muchachos at Santa Cruz de la Palma, Canary Islands, Spain. The spectra were reduced (extracted, order-merged, wavelength-calibrated) using the local HERMES pipeline (Raskin et al. 2011), and subsequently normalised using a spline fit. The spectra show strong He I 4686 lines and no sign of He I 4541 lines, indicating that the dominant signal originates from an early B star. The relative strengths of the He I and Mg lines indicates that the dominant spectral contribution is consistent with that from an O9.5-B0V star (Sota et al. 2011). The RV shifted and median combined spectrum is shown in Fig. 4, where the bottom panels show the lines used to determine the spectral classification of the star. This spectral classification agrees with the previous estimates of the spectral class by Brodskaya (1953) and Laur et al. (2017). A spectral class of O9.5-B0V nominally corresponds to a 14-17 $M_\odot$ star (Harmanec 1988; Silaj et al. 2014).

We searched for additional signals in the spectra using Least Squares Deconvolution (LSD, Donati et al. 1997; Tkachenko et al. 2013). In brief, this technique assumes that all lines in a spectrum have a common underlying profile with varying depths depending on the particular line. This common profile is recovered by deconvolving the lines within a particular wavelength region with a line-list template with associated line-depths. This method was generalised by Tkachenko et al. (2013) to allow for multiple components in a spectra and to allow for each component to draw from an different line list. Here, we calculated LSD profiles of the HERMES spectra over 4300-5200 Å. The resulting profiles did not reveal the presence of any additional components. The radial velocities of each spectrum were computed as the centre of the LSD profiles and are listed in Table A1. Inspection of the RVs reveal the same periodic signal, of P_2=52 d, as seen in the ETVs (Section 3.3).

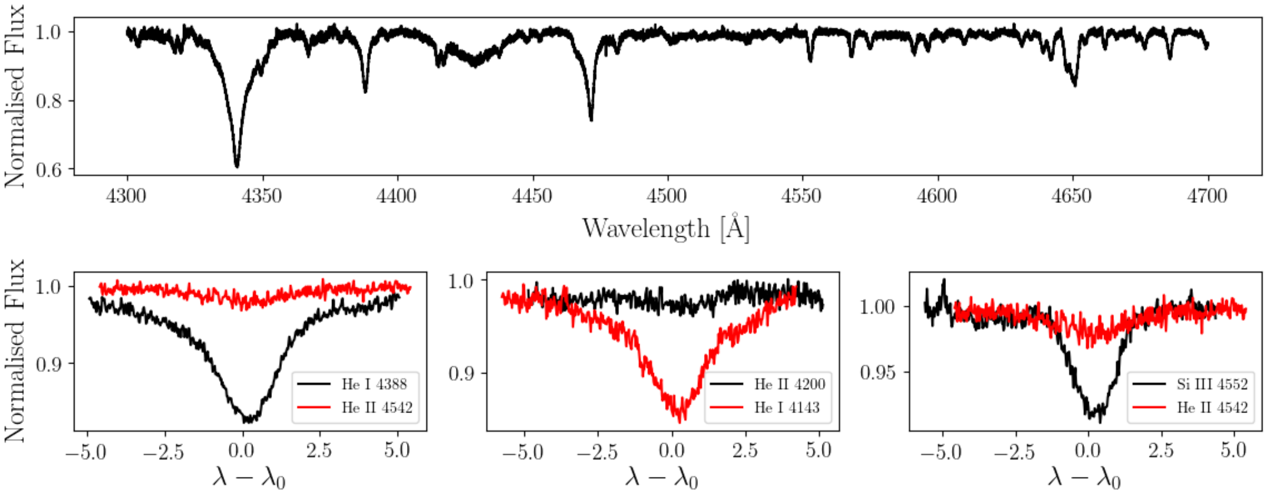

Figure 4. Top: Shifted and median combined HERMES spectra of TIC 470710327 A (SNR > 80). **Bottom**: Shifted lines used for diagnostic determination of spectral classification.

5 RV AND ETV ANALYSIS

Throughout this section we describe the joint modelling of the ETV and the RV signals assuming that they are physically associated as a triple system. As the P_2=52 d signal is seen in both the ETVs and the RVs, we confirm that the system is comprised of a P_1=1.1047 d eclipsing binary (stars A and B) and a P_2=52 d outer 9.5-B0.5V tertiary (star C) orbiting around a common centre of mass.

5.1 Joint ETV and RV modelling

The eclipse times of an isolated eclipsing binary are expected to occur at regular time intervals. However, dynamical perturbations from additional bodies, such as in a hierarchical triple system, can result in deviations from the expected times of the eclipses. There are two main effects responsible for these deviations: the light travel time effect (LTTE; geometrical contribution) and the dynamical effect. The former is a result of a change in projected distance from the centre of mass of the binary to that of the triple. The dynamical effect, on the other hand, results from physical changes in the orbit of the binary system due to the gravitational influence of the third body (Borkovits et al. 2003). Modelling of the ETVs allows us to derive properties including the mass ratio of the tertiary to the total mass of the system ($m_{\rm C}/m_{\rm ABC}$), the eccentricity of the tertiary (e_2), and the mutual inclination between the orbits of P_1 and P_2 (i_m).

Following Borkovits et al. (2016), these perturbations produce deviations to a linear ephemeris according to:

$$\Delta = \sum_{i=0}^{3} c_i E^i + \left[\Delta_{\rm LTTE} + \Delta_{\rm dyn}\right]_0^E . \quad (1)$$

The first three terms multiplied by the cycle number E represent corrections to the reference epoch (c_0), the orbital period (c_1), and any secular changes to the period (c_2).

The extent of the contribution of the LTTE to the perturbation depends on the light crossing time of the relative orbit, $a_{AB} \sin i_2/\tilde{c}$ (where $\tilde{c}$ is the speed of light), as well as the configuration of the outer orbit:

$$\Delta_{\rm LTTE} = -\frac{a_{AB} \sin i_2}{\tilde{c}} \frac{(1-e_2^2)\sin(v_2+\omega_2)}{1+e_2\cos v_2}. \quad (2)$$

Here, all quantities relating to the inner orbit $P_1 \sim 1.1$ d have a subscript 1, while all quantities relating to the outer orbit ($P_2 \sim 52$ d) have a subscript 2. Quantities with the subscript AB refer to the individual components of orbit 1, whereas quantities with the subscript C refer to the tertiary component in orbit 2. All symbols are explained in Table 2.

The dynamical perturbation has a more complex dependence on the mass ratio of the system, the ratio of the periods, as well as the mutual inclination of the two orbits, denoted as i_m. This term is given by:

$$\begin{aligned}\Delta_{\rm dyn} = &\frac{3}{4\pi}\frac{m_C}{m_{ABC}}\frac{P_1^2}{P_2}(1-e_2^2)^{-3/2} \\ &\times\left[\left(\frac{2}{3}-\sin^2 i_m\right)\mathcal{M}+\frac{1}{2}\sin^2 i_m \mathcal{S}\right]\end{aligned} \quad (3)$$

with

$$\mathcal{M} = 3e_2\sin v_2 - \frac{3}{4}{e_2}^2\sin 2v_2 + \frac{1}{3}{e_2}^3\sin 3v_2 \quad (4)$$

and

$$\mathcal{S} = \sin(2v_2+2g_2) + e_2\left[\sin(v_2+2g_2)+\frac{1}{3}\sin(3v_2+2g_2)\right]. \quad (5)$$

v_2 is the true anomaly of the outer orbit, and is determined by $T_{0,2}$, P$_2$, and e_2. All other symbols are explained in Table 2.

The RV variations of the tertiary component are given by:

$$V = \gamma + \frac{2\pi a_C \sin i_2}{P_2\sqrt{(1-e_2^2)}}[e_2\cos(\omega_2)+\cos(v_2+\omega_2)]. \quad (6)$$

Here, all terms have the same subscripts as in the ETV equations, and the systemic velocity is given by γ. Given the overlap in parameters between the ETV and RV models, as well as the complementary information held in the independent data sets, we are able to constrain the systems to a high degree.

Model optimisation was carried out using a No U-Turn Sampling (NUTS) Hamiltonian Monte Carlo (HMC) approach. In short, HMC is a class of Markov Chain Monte Carlo (MCMC) methods used to numerically approximate a posterior probability distribution. Whereas traditional MCMC techniques use a stochastic walk to explore a given n-dimensional parameter space, the NUTS algorithm makes use of a Hamiltonian description of probability distribution in order to more directly sample the posterior probability distribution of a set of model parameters θ given by Bayes' theorem: $p\,(\theta|d) \propto p\,(d|\theta,\sigma) \times p\,(\theta)$. The likelihood term $p\,(d|\theta,\sigma)$ is the evaluation of how well the model represents the data d given the parameters θ and uncertainties σ. In our application, the model is given by the ETVs and RV variations in Eqns. 1 and 6, such that:

$$p\,(d|\theta,\sigma) \propto (\mathcal{M}_{ETV} - Y_{ETV}) + (\mathcal{M}_{RV} - Y_{RV})\,, \tag{7}$$

where $\mathcal{M}$ refers to the model and Y refers to the data.

In order to best exploit the complementary and overlapping information in the RV and ETV data, the two data sets were modelled jointly. This allowed us to simultaneously fit for, and better constrain, parameters that appear in both models (see Table 2). The joint analysis made use of the open source software packages EXOPLANET and PYMC3 (Foreman-Mackey et al. 2021; Salvatier et al. 2016).The optimal parameter values and their uncertainties were calculated as the median and 67.8% highest posterior density of the marginalised posterior distributions. The priors and extracted values for all sampled parameters are given in Table 2. The best-fitting model, as constructed from the values in Table 2, for the RVs and ETVs are shown in the left and right panels of Fig. 5. We note that the residuals in the ETVs and RVs show no evidence for additional periodicities.

6 SYSTEM CONFIGURATION, STABILITY, AND EVOLUTION

6.1 Configuration

The combination of radial velocity and photometric data revealed a dynamically interacting triple system, comprised of a close 1.1047 d eclipsing binary (stars A and B) with a massive companion on a wide, non-eclipsing, ~ 52 d orbit (star C). From the dynamical modelling we derived a mass ratio of the inner binary to the tertiary of $q = m_{AB}/m_C = a_C \sin i_2 / a_{AB} \sin i_2 = 0.7776$. Given the spectral classification of star C, of O9.5V-B0.5V, the tertiary star has a mass in the range of 14-17 M$_\odot$, meaning that the combined mass of stars A and B is in the range of 10.9-13.2 M$_\odot$. The higher mass of the tertiary compared to the combined mass of the inner binary presents a rare configuration. An overview of the triple system is depicted in Fig. 6. We note that while the triple and the 0.5" companion star, TIC 470710327′, are statistically associated, the companion is not assumed to have a detectable dynamical effect on the triple.

In addition to the eclipsing P_1=1.1047 d binary signal, the *TESS* light curve contains two further periodic eclipsing signals with P_3=9.9733 d and P_4=4.092 d. Fig. 7 displays the *TESS* light curve phase folded on P_3 (top panel) and P_4 (bottom panel) after removal of the signals associated with P_1 and P_3, respectively. We note that due to the lack of visible 'secondary' eclipses, we cannot unambiguously determine whether P_3 and P_4 are the correct periods, or off by a factor of two in either direction. We can, however, determine that all three sets of eclipses are of different objects, as the morphology of all of the eclipses are constant in time, and points of overlap between the 1.10 d and 9.97 d signal are reproduced as linear additions of the different eclipse signals. Furthermore, we see no dynamical evidence in the RVs or the ETVs of either the 9.97 d or the 4.09 d signals being part of the same system. Using Eqn. 3, we can show that a dynamically interacting body with P_3=9.97 d would produce an amplitude in the ETVs that is at least $(9.97/1.10)^2 = 82$ times larger than the dynamical amplitude induced by the P_2=52 d tertiary. We see no evidence of this signal in the data. Using the same argument we also find no evidence of the P_4=4.09 d signal being associated with the tertiary star of the triple. We note that P_1=1.10 d and P_3=9.97 d is close to a 1:9 resonance. While this could indicate that the signals are related, we do not have sufficient data at present to further investigate their association.

The presence of two additional bright sources in the *TESS* aperture, at separations of 0.5" and 22", overall contributing over ~ 10% of the light in the aperture, make it difficult to determine the exact source of all of the periodic signals seen in the *TESS* light curve. Through the RVs and ETVs, however, we can associate the triple system with the brightest O9.5V-B0.5V star in the data. This is further corroborated by the data obtained with the Takahashi Epsilon telescope, which has a pixel scale of 1.64", which allowed us to confirm that the P_1=1.10 d signal lies on the O9.5V-B0.5V target star and not the 22" companion star that lies within the same *TESS* aperture.

6.2 SED Modelling

In order to investigate the properties of each component of the system we performed an analysis of the composite spectral energy distribution (SED) of TIC 470710327 and TIC 470710327', using photometric data from Vizier (Table A4). We used a pre-computed grid of solar-metallicity atmosphere models[2] with a fixed microturbulent velocity $\xi_{micro} = 2\,\mathrm{km\,s^{-1}}$ (Castelli & Kurucz 2003). The grid covers effective temperatures, T_eff, in the range of 3000 K - 50 000 K, with ΔT_eff = 250 K for $T_\mathrm{eff} \leq$ 13 000 K and ΔT_eff = 1000 K for $T_\mathrm{eff} \geq$ 13 000 K. While the grid spans a wide range in $\log g$, we make the assumption that all components have $\log g = 4.0$ and only use these models. The models were reddened according to $F_\mathrm{red} = 10^{-A/2.5} F_\mathrm{mod}$ and $A = E(B-V)R$, where E(B-V) was a free parameter, and R was calculated according to Cardelli et al. (1989). Each model was evaluated against the data using a χ^2 metric.

We fit a composite four-component SED to the observations, assuming one component for each member of the triple system, and one for the nearby 0.5" companion, TIC 470710327′. The light contributions derived in Section 3 were used to inform the model, such that the total light contribution of the triple system was fixed to 77% in the V-band, with the remaining 23% originating from TIC 470710327′. Additionally, the model enforced that the luminosity of the primary component of the close binary must be higher than that of the secondary. Using stellar radii derived for the range of possible stellar masses $m_C \in 14-17\ M_\odot$ and assuming $\log g = 4.0$ dex, the luminosity of the tertiary was calculated for each effective temperature from the grid. The distance of the system was then scaled such that the luminosity of star C is consistent with luminosities expected for stars with a mass in the range of 14-17 M$_\odot$ (REF). With the distance and the light ratios fixed, we were able to calculate a range of masses and temperatures for the components of the close binary that satisfied the triple system mass ratio. Only solutions that satisfied the triple system mass-ratio of $q_c = 0.776$ were retained.

The solutions favour masses of the OB star of 14-15 M$_\odot$, whereas the solutions for the components of the close binary orbit favour a mass ratio $q_1 \in 0.9-1.0$ with masses for the primary components ranging from 5.1 to 6 M$_\odot$. We find several suitable

---

[2] Models are available at `https://wwwuser.oats.inaf.it/castelli/grids.html`

Table 2. System parameters either sampled or derived from the HMC optimisation, as well as parameters estimated from the *TESS* light curve.

Parameter	Symbol	Prior	Value	Units	Model
Sampled parameters					
Orbital period tertiary	P_2	$\mathcal{N}[52.1, 2]$	$52.044^{+0.017}_{-0.017}$	days	ETV + RV
Semi-major axis, binary to COM	$a_{\rm AB} \sin i_2$	$\mathcal{U}[10, 500]$	$91.22^{+2.671}_{-10.65}$	$R_\odot$	ETV
Tertiary to total mass ratio ($m_{\rm C}$ / $m_{\rm ABC}$)	$q_{\rm tot}$	$\mathcal{N}[0.58, 0.14]$	$0.563^{+0.032}_{-0.014}$		ETV
Eccentricity	e_2	$\mathcal{U}[0, 0.4]$	$0.30^{+0.013}_{-0.009}$		ETV + RV
Observed argument of periastron	ω_2	$\mathcal{U}[0, 2\pi]$	$-1.123^{+0.115}_{-0.063}$	rad	ETV + RV
Mutual inclination	i_m	$\mathcal{U}[0, 2\pi]$	$0.294^{+0.073}_{-0.024}$	rad	ETV
Dynamical argument of periastron	g_2	$\mathcal{U}[0, 2\pi]$	$-0.017^{+0.21}_{-0.718}$	rad	ETV
Semi-amplitude	$\log K$	$\mathcal{N}[81, 20]$	$4.279^{+0.023}_{-0.019}$]		RV
t_0 of tertiary	$t_{0,2}$	$\mathcal{N}[1878, 25]$	$1880.394^{+0.713}_{-0.267}$	BJD - 2457000	ETV + RV
Correction to T_0	c_0	$\mathcal{N}[0, 5]$	$-0.0^{+0.0}_{-0.0001}$		ETV
Correction to P_1	c_1	$\mathcal{N}[0, 0.5]$	$-0.003^{+0.017}_{-0.009}$		ETV
Secular change to P_1	c_2	$\mathcal{N}[0, 0.0001]$	$0.237^{+0.521}_{-0.275}$		ETV
Derived parameters					
Semi-major axis, tertiary to COM	$a_{\rm C} \sin i_2$	–	$70.923^{+0.98}_{-2.03}$	$R_\odot$	RV
Project mass of binary	$m_{\rm AB} \sin^3 i_2$	–	$9.21^{+0.6}_{-1.4}$	$M_\odot$	ETV + RV
Project mass of tertiary	$m_{\rm C} \sin^3 i_2$	–	$11.87^{+0.9}_{-2.9}$	$M_\odot$	ETV + RV
Light curve extracted parameters					
Orbital period binary	P_1	–	1.104686±0.000004 d	days	–
t_0 of primary	$t_{0,1}$	–	1785.533	BJD - 2457000	–

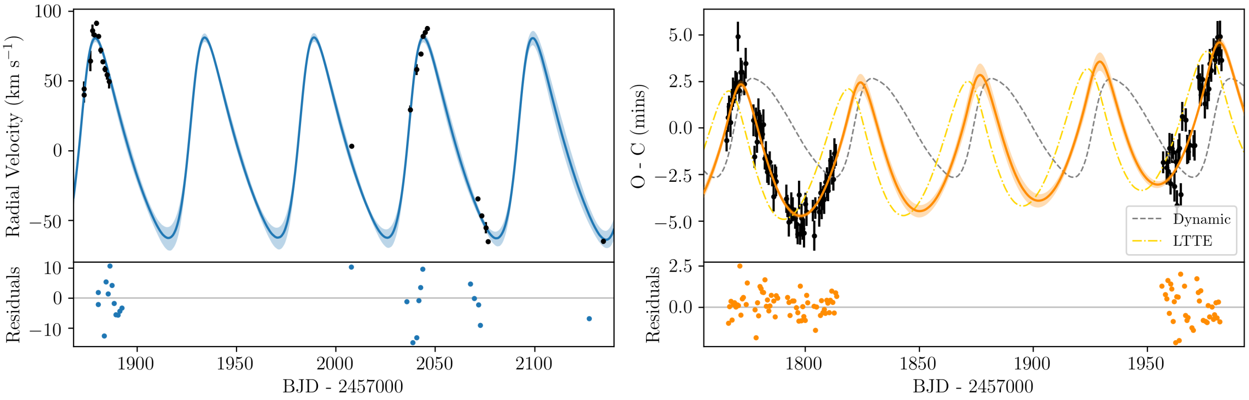

Figure 5. Joint MCMC model of the HERMES RV data (left panel) and the extracted eclipse timing variations (right panel). The model parameters are presented in Table 2. The bottom panels show the residuals of the best fit. The overall ETV fit is a linear addition of the dynamical effect (small dashed grey line) and the light travel time effect (large dashed yellow line).

solutions for the nearby companion, and as such make no further comment on its nature.

6.3 Dynamical stability

Even though both the inner and outer orbits of the triple system are relatively compact, the separation between the two orbits ($P_2/P_1 \approx 50$) implies that the current configuration is dynamically stable. The stability criterion of Mardling & Aarseth (1999), implies long-term dynamical stability for TIC 470710327 for $P_2 \gtrsim 18$ d.

Dynamically stable systems can remain intact for many dynamical timescales, giving rise to the possibility of observing three-body dynamics. ZKL cycles (Lidov 1962; Kozai 1962), for example, would manifest themselves as cyclic changes in the eccentricity of the inner orbit and in the mutual inclination between the inner and outer orbit. However, classical ZKL resonance can only occur in triples with mutual inclinations between 39.2° and 140.8°, meaning that with the mutually inclined of TIC 470710327, of $\approx 16.8^{+4.18}_{-1.38}$ °, this effect is unlikely to be significant for the future evolution of the system.

Conversely, the higher-order effects of three-body dynamics could affect the dynamical evolution of this system. The eccentric

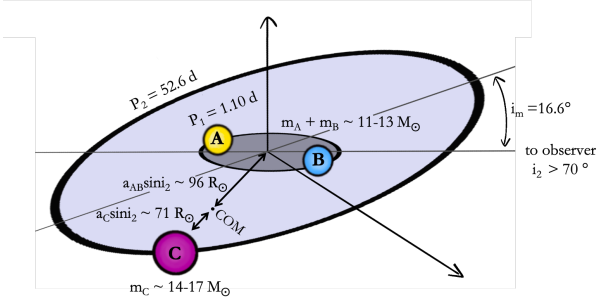

Figure 6. Schematic of the triple system. Relative sizes of the orbits are not to scale and for simplicity the orbits are depicted as circular.

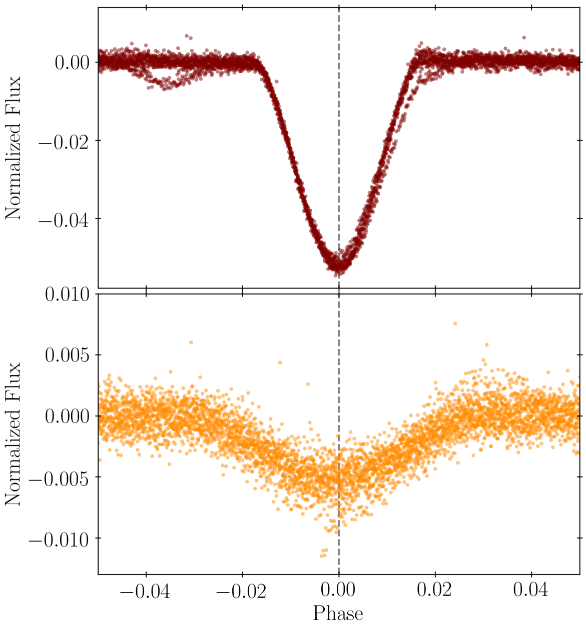

Figure 7. TESS light curve phase folded at periods of P_4 = 9.9733 d (top panel) and P_3 = 4.1 d (bottom panel).

ZKL mechanism (eZKL; see Naoz 2016, for a review) can give rise to more extreme eccentricity cycles for an extended range of inclinations. The magnitude of this effect can be quantified with the use of the octupole parameter (Lithwick & Naoz 2011; Katz et al. 2011; Teyssandier et al. 2013; Li et al. 2014):

$$\epsilon_{\rm oct} \equiv \frac{m_{\rm A} - m_{\rm B}}{m_{\rm A} + m_{\rm B}} \frac{a_1}{a_2} \frac{e_2}{1 - e_2^2} \equiv \frac{1 - q_1}{1 + q_1} \sqrt[3]{\frac{P_1^2}{P_2^2}(1 - q_{\rm tot})} \frac{e_2}{1 - e_2^2}. \quad (8)$$

The eZKL mechanism is expected to be important for the evolution of the system for values of $\epsilon_{\rm oct} \gtrsim 0.001 - 0.01$, and under the condition that the mass ratio of the inner binary is less than unity. Given the values in Table 2, we find $\epsilon_{\rm oct}$=0.001 for $q \approx 0.9$ and $\epsilon_{\rm oct}$=0.01 for $q \approx 0.3$. Given the morphology of the eclipses in the *TESS* data (and considering the substantial diluting third light), initial modelling suggests that the mass ratio of this inner binary is $q \approx 0.85 - 0.9$, which is consistent with the results of the composite SED modelling. Thus, the octopole term is within the range of relevance for the dynamical evolution of this system. The expected timescale of the eZLK cycles are thought to be of order $\tau \approx 180$ yr / $\sqrt{\epsilon_{\rm oct}}$ (Antognini 2015). However, further constraining of the mass ratio of the inner binary requires detection of their radial velocities.

6.4 Possible formation scenarios

Several theories exist pertaining to the origin of higher order multiple systems. The formation of multiple systems is dependent on fragmentation of the natal material during the formation process. Hierarchical collapse within molecular clouds eventually leads to the formation of dense stellar cores and clumps, whose collapse results in the formation of stars and clusters. Throughout this, equatorial discs are formed through the conservation of angular momentum, which in turn can become involved in the accretion process and the formation of secondary cores. However, there is still debate as to what scale of fragmentation is the main cause of observed massive multiple systems - the fragmentation of the prestellar core or fragmentation of circumstellar discs. In both cases, opacity has a large effect on the initial separations of the systems, which cannot be less than around 10 au due to the opacity limit of fragmentation (Boss 1998, Bate 1998). Therefore it is assumed that systems at closer separations than 10 au must have migrated to their observed positions (Bate et al. 2002). Some studies present evidence of disc fragmentation creating higher order massive multiple systems during their embedded phases (e.g. Megeath et al. 2005). Other effects such as dynamical interactions between other companions and discs (Eggleton & Kisseleva-Eggleton 2006) could also cause inner binaries in multiple systems to harden into close orbits. Recent modelling by Oliva & Kuiper (2020), for example, has shown how disc fragments in the discs of massive protostars form through hierarchical fragmentation along spiral arms and migrate to spectroscopic orbits.

TIC 470710327 presents an interesting puzzle in terms of its formation given our derived geometry of a close binary with a total mass lower than the tertiary star. More massive stars have shorter Kelvin-Helmholtz timescales than those of lower masses, so one would expect that the more massive tertiary was the first star to form. However, if this was the case, it is likely that when this star reached the main sequence (before the inner binary) it would have disrupted the remaining natal material and therefore discontinued the central binary's formation. If the central binary did form first, a more consistent interpretation could be that the inner binary formed through disc fragmentation and the dynamical effects of this binary on the disc could have created a large over-density at large radii. Such over-densities have been shown to occur in circumbinary discs in works such as Price et al. (2018). This over-density could have accreted significant mass, perhaps accelerated by the continuing dynamical effects of the inner binary. In order for this scenario to hold the mass of the disc must have been very large, as the disc fragmentation process would not convert all the disc material into the eventual stars, and the combined mass of the stars in the tertiary system is at least 29 solar masses. However, the largest protostellar discs detected around massive young stellar objects are of order $\sim$10M$_\odot$ (e.g. Johnston et al. 2020, Frost et al. 2021).

An alternative explanation for the formation of TIC 470710327 is that this system is a result of the fragmentation of the prestellar core as opposed to fragmentation of a disc. This is supported by the fact that additional sources surround this triple system in the local region, in the form of a 0.5" and a ~ 22" away companion. With a spurious association probability of ~ 1×10^{-5} between TIC 470710327 and the 0.5" companion, this closer source is expected to have formed from the same core collapse. While the more distant source at ~ 22" may not be currently bound to the tertiary system, it could still have come from the same prestellar core. The core collapse scenario circumvents the mass problem described above for disc fragmentation. Should this have occurred, we can assume that the close-binary formed from one collapse event, the tertiary star from another and the distant source from yet another. The close-binary system could have been formed by disc fragmentation as described above, and its hardening into a close-orbit could have been facilitated by dynamical interactions between the 14-17M$_\odot$ star and the distant sources from others. Dynamical effects within the collapsing core could also have led to the capture of the 14-17M$_\odot$ star by the close-binary system, forming the tertiary we see today. Dedicated radiative hydrodynamical modelling could help disentangle whether core fragmentation, disc fragmentation or a combination of both resulted in the formation of TIC 470710327, whilst repeat observations of the all the sources of the region could help distinguish orbits and determine which stars are bound. Furthermore, as there are currently no resolved Gaia parallaxes for TIC 470710327 and TIC 470710327′, we cannot concretely rule out the possibility that these are just un-associated nearby objects on the sky.

6.5 Future evolution

The derived mass ratio, whereby the tertiary is more massive than the combined mass of the inner binary, makes TIC 470710327 stand out as a rare system. In triple systems the outer star is typically less massive than the combined mass of the inner binary, and often less massive than the primary star alone (Tokovinin 2014; Moe & Di Stefano 2017). As a result of the outer star (m_C) being more massive than the combined mass of the inner binary ($m_{\rm AB}$), the outer star has the shortest evolutionary timescale and will be the first to evolve off the main-sequence. Given the expected mass of the tertiary of 14-17 M$_\odot$, star C is expected to fill its Roche lobe at an age of $\sim$ 13 Myr, at which point it will start transferring mass towards the inner binary. This type of mass transfer, from an outer star to an inner binary, is expected to occur in $\sim$ 1% of all triple systems in the Massive Star Catalogue (de Vries et al. 2014).

The outcome of such a mass transfer phase is, inherently, a hydrodynamical problem (de Vries et al. 2014; Portegies Zwart & Leigh 2019). If the inner binary is compact enough such that the mass transfer stream intersects itself, a circumbinary disk may form. Leigh et al. (2020b) argue that such a scenario leads to preferential accretion to the lowest mass star of the inner binary and therefore favours evolution towards equal mass inner binary stars. The circularisation radius of the mass transfer material (Frank et al. 2002; Toonen et al. 2016) is around 20$R_\odot$. As the inner binary has an orbital separation of $\sim$ 10$R_\odot$, a disk may form, but it is not clear from simple analytical calculation whether that disk would be stable enough to warrant secular accretion. If the mass transfer stream intersects the trajectory of the inner two stars in their orbit around each other, friction may reduce the orbit (de Vries et al. 2014) to lead to a contact system and/or a merger. Such a merger remnant may be considered a blue straggler in twofold: it would be rejuvenated due to the merger as well as due to the accretion from the tertiary star.

Assuming a merger does take place, the triple would reduce to a binary system (stage 3 in Fig 8). After the mass transfer phase ends the merger remnant would have a mass of 12-18 $M_\odot$ depending on how efficiently the binary was able to accrete matter. Given the mass of the former donor star it will evolve to become a neutron star. With typical post-mass transfer periods of several hundreds of days (i.e. orbital velocities of around 100 km/s), typical natal kicks from the supernova explosion, with magnitudes of several hundreds of km/s, would unbind the newly formed binary into two single stars (Hobbs et al. 2005; Verbunt et al. 2017; Igoshev 2020), reducing the multiplicity of the system once more (5a in Fig 8). If the orientation of the supernova kick is such that the binary remains intact the binary would likely undergo an additional mass transfer phase when the merger remnant evolves off the main-sequence. Given the large mass ratio of such a binary, the mass transfer would lead to a common-envelope phase (Ivanova et al. 2013). Consequently, this could either lead to a merger and the formation of a Thorn-Zytkow object (whereby the neutron star is enclosed by the red giant star, 6a in Fig 8 Thorne & Zytkow 1975; Podsiadlowski et al. 1995; Levesque et al. 2014; Tabernero et al. 2021) or, if the binary survives, experience an ultra-stripped supernova (Tauris 2015) and end up as a double neutron-star (6b in Fig 8).

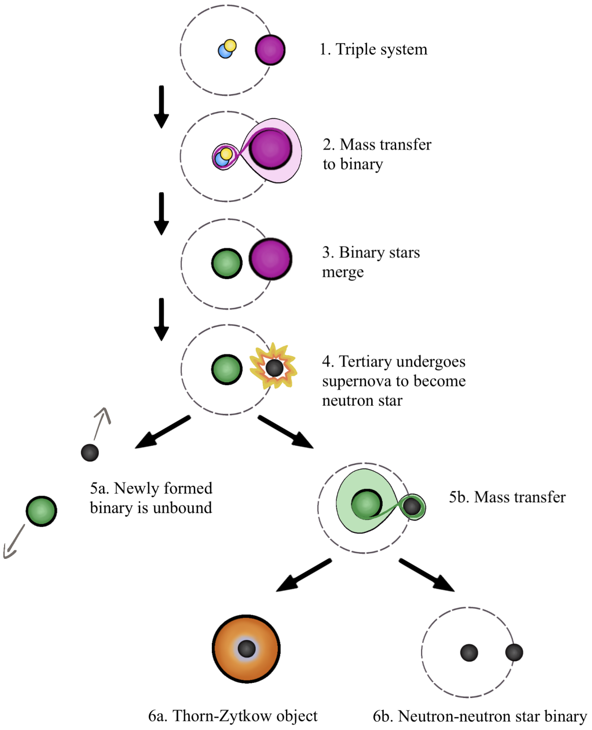

Figure 8. Possible future evolution of TIC 470710327. Relative sizes of the stars and orbits are not to scale. For simplicity, all orbits are depicted as circular.

7 CONCLUSIONS

TIC 470710327 is a compact, hierarchical triple system consisting of a 1.10 d binary and a 52 d tertiary. The system was initially identified in *TESS* data by citizen scientists taking part in the Planet Hunters TESS project. Using publicly available *TESS* data and newly obtained HERMES data, we report on the dynamical modelling of the system to reveal a rare configuration wherein the tertiary object in the wide orbit is more massive than the combined mass of the inner binary ($m_{\rm AB}$=10.9 - 13.2 M$_\odot$, $m_{\rm C}$=14 - 17 M$_\odot$). This configuration poses several challenges to explain its formation.

Given the compact orbits and the unusually high mass of the tertiary object, we speculate that the future evolution of this system will minimally involve one episode of mass transfer as the massive tertiary evolves across the Hertzsprung gap. Based on its initial mass, the tertiary will likely end its life as a neutron star. Alternatively, depending on the rate and efficiency of the mass transfer to the inner binary, the tertiary could evolving into an intermediate mass stripped star (Götberg et al. 2020). Should the binary system remain bound after the expected supernova(e) kick(s), this system could result in a close double neutron star gravitational wave progenitor, or an exotic Thorn-Zytkow object. Detection of more systems similar to TIC 470710327 would provide constraints on potential progenitor systems to gravitational wave events.

In addition to the triple system we report on two nearby stars that significantly contribute to the *TESS* aperture, located at angular separations of 22" (LS I +61 72) and 0.5" (TIC 470710327′). Given the field density of stars around TIC 470710327, determined using Gaia eDR3, and the magnitude contrast between the target and the 0.5" companion, we show that the spurious association probability between TIC 470710327 and TIC 470710327′ is $\sim\ 1\times10^{-5}$. These two nearby stars may be the source of the two additional periodic signals (P_3 = 9.97 d and P_4 = 4.01 d) seen in the *TESS* light curve. Additional photometric observations of the nearby stars are needed in order to probe the origins of the P_3 and P_4 and to determine the true multiplicity of this complex system.

With further observational characterisation, particularly aimed at characterising the nature of the inner binary, this system stands to become an excellent target to scrutinise simulations of massive star formation and evolution. Future spectroscopic observations that are specifically aimed at detecting the RV variations of both components of the inner binary would allow us to place tighter constraints on the dynamics of the system. In particular, these observations would allow us to probe the eZKL mechanism. Finally, RV characterisation and detailed eclipse modelling of the inner binary would precisely constrain the light contributions of all components of the triple system. With such constraints, derivation of the atmospheric properties, such as $T_{\rm eff}$, $\log g$, $v_{\rm rot}$ and $L_{\rm bol}$ would allow us to further test whether the three stars are coeval.

DATA AVAILABILITY

The *TESS* data used within this article are hosted and made publicly available by the Mikulski Archive for Space Telescopes (MAST, `http://archive.stsci.edu/tess/`). The *TESS* data described here may be obtained from `https://dx.doi.org/10.17909/t9-5z05-k040`. Similarly, the Planet Hunters TESS classifications made by the citizen scientists can be found on the Planet Hunters Analysis Database (PHAD, `https://mast.stsci.edu/phad/`), which is also hosted by MAST.

Original sc Hermes spectra, and the newly obtained photometric data are available upon request.

ACKNOWLEDGEMENTS

We thank all of the citizen scientists who take part in the Planet Hunters TESS project and who enable the discovery of exciting planet and stellar systems in TESS data. NE also thanks the LSSTC Data Science Fellowship Program, which is funded by LSSTC, NSF Cybertraining Grant number 1829740, the Brinson Foundation, and the Moore Foundation; her participation in the program has benefited this work. Furthermore, NE and SA acknowledge support from the UK Science and Technology Facilities Council (STFC)under grant codes ST/R505006/1 and consolidated grant no. ST/S000488. This work also received funding from the European Research Council (ERC) under the European Union's Horizon 2020 research and innovation program (Grant agreement No. 865624). CJ has received funding from the Research Foundation Flanders under grant agreement G0A2917N (BlackGEM). ST acknowledge support from the Netherlands Research Council NWO (VENI 639.041.645 grants).

Some of the data presented in this paper were obtained from the Mikulski Archive for Space Telescopes (MAST). STScI is operated by the Association of Universities for Research in Astronomy, Inc., under NASA contract NAS5-26555. Support for MAST for non-HST data is provided by the NASA Office of Space Science via grant NNX13AC07G and by other grants and contracts. This paper includes data collected with the TESS mission, obtained from the MAST data archive at the Space Telescope Science Institute (STScI). Funding for the TESS mission is provided by the NASA Explorer Program. STScI is operated by the Association of Universities for Research in Astronomy, Inc., under NASA contract NAS 5–26555.

REFERENCES

Aldoretta E. J., et al., 2015, AJ, 149, 26
Altmann M., Roeser S., Demleitner M., Bastian U., Schilbach E., 2017, VizieR Online Data Catalog, p. I/339
Ammons S. M., Robinson S. E., Strader J., Laughlin G., Fischer D., Wolf A., 2010, VizieR Online Data Catalog, p. V/136
Antognini J. M. O., 2015, MNRAS, 452, 3610
Antonini F., Toonen S., Hamers A. S., 2017, ApJ, 841, 77
Barbary K., 2016, The Journal of Open Source Software, 1, 58
Bastian N., Covey K. R., Meyer M. R., 2010, ARA&A, 48, 339
Bate M. R., 1998, ApJ, 508, L95
Bate M. R., Bonnell I. A., Bromm V., 2002, MNRAS, 336, 705
Bertin E., Arnouts S., 1996, A&AS, 117, 393
Bodensteiner J., et al., 2021, arXiv e-prints, p. arXiv:2104.13409
Borkovits T., Érdi B., Forgács-Dajka E., Kovács T., 2003, A&A, 398, 1091
Borkovits T., Rappaport S., Hajdu T., Sztakovics J., 2015, MNRAS, 448, 946
Borkovits T., Hajdu T., Sztakovics J., Rappaport S., Levine A., Bíró I. B., Klagyivik P., 2016, MNRAS, 455, 4136
Borkovits T., et al., 2021, MNRAS, 503, 3759
Boss A. P., 1998, ApJ, 501, L77
Bourges L., Mella G., Lafrasse S., Duvert G., Chelli A., Le Bouquin J. B., Delfosse X., Chesneau O., 2017, VizieR Online Data Catalog, p. II/346
Brodskaya E. S., 1953, Izvestiya Ordena Trudovogo Krasnogo Znameni Krymskoj Astrofizicheskoj Observatorii, 10, 104
Cardelli J. A., Clayton G. C., Mathis J. S., 1989, ApJ, 345, 245
Castelli F., Kurucz R. L., 2003, in Piskunov N., Weiss W. W., Gray D. F., eds, Vol. 210, Modelling of Stellar Atmospheres. p. A20 (`arXiv:astro-ph/0405087`)
Conroy K. E., Prša A., Stassun K. G., Orosz J. A., Fabrycky D. C., Welsh W. F., 2014, AJ, 147, 45
Cutri R. M., et al. 2013, VizieR Online Data Catalog, p. II/328
Cutri R. M., et al., 2003, VizieR Online Data Catalog, p. II/246
Dib S., Schmeja S., Hony S., 2017, MNRAS, 464, 1738
Donati J. F., Semel M., Carter B. D., Rees D. E., Collier Cameron A., 1997, MNRAS, 291, 658
Droege T. F., Richmond M. W., Sallman M., 2007, VizieR Online Data Catalog, p. II/271A
Eggleton P. P., Kisseleva-Eggleton L., 2006, Ap&SS, 304, 75
Eisner N. L., et al., 2020, arXiv e-prints, p. arXiv:2011.13944
Fabricius C., Høg E., Makarov V. V., Mason B. D., Wycoff G. L., Urban S. E., 2002, A&A, 384, 180
Foreman-Mackey D., et al., 2021, exoplanet-dev/exoplanet v0.4.5, doi:10.5281/zenodo.1998447, `https://doi.org/10.5281/zenodo.1998447`
Frank J., King A., Raine D. J., 2002, Accretion Power in Astrophysics: Third Edition. Accretion Power in Astrophysics, Cambridge University Press

Frost A. J., Oudmaijer R. D., de Wit W. J., Lumsden S. L., 2021, arXiv e-prints, p. arXiv:2102.05087
Gaia Collaboration Brown A. G. A., Vallenari A., Prusti T., de Bruijne J. H. J., Babusiaux C., Biermann M., 2020, arXiv e-prints, p. arXiv:2012.01533
Gaia C., et al., 2018, Astronomy & Astrophysics, 616
Glanz H., Perets H. B., 2021, MNRAS, 500, 1921
Götberg Y., Korol V., Lamberts A., Kupfer T., Breivik K., Ludwig B., Drout M. R., 2020, ApJ, 904, 56
Hajdu T., Borkovits T., Forgács-Dajka E., Sztakovics J., Marschalkó G., Benkő J. M., Klagyivik P., Sallai M. J., 2017, MNRAS, 471, 1230
Hamers A. S., Rantala A., Neunteufel P., Preece H., Vynatheya P., 2021, MNRAS, 502, 4479
Harmanec P., 1988, Bulletin of the Astronomical Institutes of Czechoslovakia, 39, 329
Hartkopf W. I., et al., 2000, AJ, 119, 3084
Hartkopf W. I., Mason B. D., Rafferty T. J., 2008, AJ, 135, 1334
Henden A. A., Templeton M., Terrell D., Smith T. C., Levine S., Welch D., 2016, VizieR Online Data Catalog, p. II/336
Hobbs G., Lorimer D. R., Lyne A. G., Kramer M., 2005, MNRAS, 360, 974
Howell S. B., Everett M. E., Sherry W., Horch E., Ciardi D. R., 2011, AJ, 142, 19
Igoshev A. P., 2020, MNRAS, 494, 3663
Ito T., Ohtsuka K., 2019, Monographs on Environment, Earth and Planets, 7, 1
Ivanova N., et al., 2013, A&ARv, 21, 59
Jenkins J. M., et al., 2016, in Proc. SPIE. p. 99133E, doi:10.1117/12.2233418
Johnston K. G., et al., 2020, A&A, 634, L11
Katz B., Dong S., Malhotra R., 2011, Physical Review Letters, 107, 181101
Kiminki D. C., Kobulnicky H. A., 2012, ApJ, 751, 4
Kozai Y., 1962, AJ, 67, 591
Lasker B., Lattanzi M. G., McLean B. J., et al. 2007, VizieR Online Data Catalog, p. I/305
Laur J., Kolka I., Eenmäe T., Tuvikene T., Leedjärv L., 2017, A&A, 598, A108
Leigh N. W. C., Toonen S., Portegies Zwart S. F., Perna R., 2020a, MNRAS, 496, 1819
Leigh N. W. C., Toonen S., Portegies Zwart S. F., Perna R., 2020b, MNRAS, 496, 1819
Levesque E. M., Massey P., Zytkow A. N., Morrell N., 2014, MNRAS, 443, L94
Li G., Naoz S., Holman M., Loeb A., 2014, ApJ, 791, 86
Li M. C. A., et al., 2018, MNRAS, 480, 4557
Lidov M. L., 1962, Planet. Space Sci., 9, 719
Lintott C. J., et al., 2008, MNRAS, 389, 1179
Lintott C., et al., 2011, MNRAS, 410, 166
Lithwick Y., Naoz S., 2011, ApJ, 742, 94
Maíz Apellániz J., et al., 2019, A&A, 626, A20
Mardling R., Aarseth S., 1999, in Steves B. A., Roy A. E., eds, NATO Advanced Science Institutes (ASI) Series C Vol. 522, NATO Advanced Science Institutes (ASI) Series C. p. 385
Marsh T. R., Armstrong D. J., Carter P. J., 2014, MNRAS, 445, 309
Matson R. A., Howell S. B., Ciardi D. R., 2019, AJ, 157, 211
Megeath S. T., Wilson T. L., Corbin M. R., 2005, ApJ, 622, L141
Moe M., Di Stefano R., 2017, ApJS, 230, 15
Naoz S., 2016, ARA&A, 54, 441
Oliva G. A., Kuiper R., 2020, A&A, 644, A41
Podsiadlowski P., Cannon R. C., Rees M. J., 1995, MNRAS, 274, 485
Pollacco D. L., et al., 2006, PASP, 118, 1407
Portegies Zwart S., Leigh N. W. C., 2019, ApJ, 876, L33
Price D. J., et al., 2018, MNRAS, 477, 1270
Rainot A., et al., 2020, A&A, 640, A15
Rappaport S., et al., 2017, MNRAS, 467, 2160
Raskin G., et al., 2011, A&A, 526, A69
Reed B. C., 2003, AJ, 125, 2531
Renzo M., et al., 2019, A&A, 624, A66
Ricker G. R., et al., 2015, Journal of Astronomical Telescopes, Instruments, and Systems, 1, 014003
Salpeter E. E., 1955, ApJ, 121, 161
Salvatier J., Wiecki T. V., Fonnesbeck C., 2016, PeerJ Computer Science, 2, e55
Sana H., et al., 2012, Science, 337, 444
Sana H., et al., 2013, A&A, 550, A107
Sana H., et al., 2014, ApJS, 215, 15
Silaj J., Jones C. E., Sigut T. A. A., Tycner C., 2014, ApJ, 795, 82
Sota A., Maíz Apellániz J., Walborn N. R., Alfaro E. J., Barbá R. H., Morrell N. I., Gamen R. C., Arias J. I., 2011, ApJS, 193, 24
Sriram K., Malu S., Choi C. S., Vivekananda Rao P., 2018, AJ, 155, 172
Stephan A. P., et al., 2019, ApJ, 878, 58
Tabernero H. M., Dorda R., Negueruela I., Marfil E., 2021, A&A, 646, A98
Tan J. C., Beltrán M. T., Caselli P., Fontani F., Fuente A., Krumholz M. R., McKee C. F., Stolte A., 2014, in Beuther H., Klessen R. S., Dullemond C. P., Henning T., eds, Protostars and Planets VI. p. 149 (`arXiv:1402.0919`), doi:10.2458/azu_uapress_9780816531240-ch007
Tauris T., 2015, arXiv e-prints, p. arXiv:1510.07875
Teyssandier J., Naoz S., Lizarraga I., Rasio F. A., 2013, ApJ, 779, 166
Thorne K. S., Zytkow A. N., 1975, ApJ, 199, L19
Tkachenko A., Van Reeth T., Tsymbal V., Aerts C., Kochukhov O., Debosscher J., 2013, A&A, 560, A37
Tokovinin A., 2014, AJ, 147, 87
Toonen S., Hamers A., Portegies Zwart S., 2016, Computational Astrophysics and Cosmology, 3, 6
Verbunt F., Igoshev A., Cator E., 2017, A&A, 608, A57
Zacharias N., Finch C. T., Girard T. M., Henden A., Bartlett J. L., Monet D. G., Zacharias M. I., 2012, VizieR Online Data Catalog, p. I/322A
Zinnecker H., Yorke H. W., 2007, ARA&A, 45, 481
de Mink S. E., Langer N., Izzard R. G., Sana H., de Koter A., 2013, ApJ, 764, 166
de Vries N., Portegies Zwart S., Figueira J., 2014, MNRAS, 438, 1909

APPENDIX A: ADDITIONAL TABLES

Summary of the RV observations obtained with the HERMES spectrograph (Section 4), ETVs determined from the TESS data (Section 3.3 and inputs used for the SED analysis (Section 6.2).

This paper has been typeset from a TEX/LATEX file prepared by the author.

Time (BJD - 2457000)	RV (km/s)	RV err (km/s)	SNR
1880.3395	0.03	5.55	45
1880.3518	4.22	5.47	45
1883.3908	24.25	7.35	27
1884.3813	46.12	4.15	59
1885.3333	43.12	1.49	85
1886.3368	51.28	2.02	80
1887.3369	42.11	0.90	91
1888.3537	32.07	2.45	75
1889.3285	23.70	1.11	89
1890.3321	18.43	2.19	78
1891.3247	14.30	3.45	66
1892.3270	9.70	5.30	47
2007.7168	-36.85	0.84	92
2035.6305	-10.77	2.99	70
2038.6952	18.08	4.00	60
2040.6938	29.27	0.79	92
2041.6919	42.08	0.80	92
2042.6432	44.82	1.55	85
2043.6680	47.71	1.58	84
2067.7128	-74.50	0.88	91
2069.7160	-86.61	0.87	91
2071.7410	-95.40	4.04	60
2072.7397	-105.13	0.39	96
2127.5437	-105.09	1.85	82

Table A1. RV observations for TIC 470710327

Cycle number	Predicted linear ephemeris epoch (BJD - 2457000)	O-C (mins)	(mins) (mins)
0	1766.2700	-0.684	0.582
1	1767.3747	1.147	0.583
2	1768.4794	1.51	0.577
3	1769.5841	1.908	0.594
4	1770.6887	2.403	0.592
5	1771.7934	1.995	0.59
6	1772.8981	3.012	0.604
7	1774.0028	2.351	0.603
11	1778.4215	-1.554	0.599
12	1779.5262	-0.756	0.584
13	1780.6309	0.378	0.581
14	1781.7356	-0.343	0.609
15	1782.8403	-1.649	0.589
16	1783.9450	-2.364	0.602
17	1785.0497	-1.846	0.58
18	1786.1543	-2.562	0.594
19	1787.2590	-2.571	0.598
24	1792.7825	-4.193	0.599
25	1793.8871	-10.852	0.597
26	1794.9918	-4.375	0.644
27	1796.0965	-4.856	0.577
28	1797.2012	-5.707	0.563
29	1798.3059	-5.709	0.575
30	1799.4106	-5.429	0.591
31	1800.5153	-4.098	0.605
34	1803.8293	-4.444	0.581
35	1804.9340	-4.312	0.584
36	1806.0387	0.786	0.554
37	1807.1434	-3.49	0.568
38	1808.2480	-3.775	0.649
39	1809.3527	-2.923	0.562
40	1810.4574	-3.381	0.563
41	1811.5621	-1.754	0.566
42	1812.6668	-2.763	0.608
43	1813.7715	-1.453	0.587
172	1956.2759	-1.853	0.587
174	1958.4853	-2.323	0.625
175	1959.5900	-3.002	0.59
176	1960.6946	-1.307	0.591
177	1961.7993	-1.815	0.592
178	1962.9040	-1.221	0.594
179	1964.0087	-3.575	0.594
181	1966.2181	0.422	0.629
182	1967.3228	-1.289	0.599
184	1969.5321	-0.969	0.583
186	1971.7415	2.736	0.627
187	1972.8462	1.779	0.615
188	1973.9509	-3.132	0.593
190	1976.1602	2.088	0.657
191	1977.2649	3.076	0.611
192	1978.3696	4.212	0.594
193	1979.4743	4.072	0.623
194	1980.5790	3.98	0.597
195	1981.6837	3.632	0.582

Table A2. O-C values for the primary eclipses.

Cycle number	Predicted linear ephemeris epoch (BJD - 2457000)	O-C (mins)	(mins) (mins)
0.5	1766.8223	0.552	0.773
1.5	1767.9270	0.284	0.775
2.5	1769.0317	1.908	0.789
3.5	1770.1364	2.266	0.805
4.5	1771.2411	4.902	0.796
5.5	1772.3458	2.988	0.786
6.5	1773.4505	-4.964	0.792
7.5	1774.5551	3.468	0.821
10.5	1777.8692	0.403	0.850
11.5	1778.9739	0.303	0.784
12.5	1780.0786	0.757	0.829
13.5	1781.1833	-0.089	0.791
14.5	1782.2879	0.185	0.807
15.5	1783.3926	-1.492	0.779
16.5	1784.4973	-2.271	0.794
18.5	1786.7067	-3.702	0.791
19.5	1787.8114	-2.883	0.804
23.5	1792.2301	-3.806	0.763
24.5	1793.3348	-5.062	0.774
25.5	1794.4395	-4.309	0.836
27.5	1796.6489	-5.181	0.763
28.5	1797.7535	-3.611	0.768
29.5	1798.8582	-4.852	0.784
30.5	1799.9629	-5.658	0.776
31.5	1801.0676	-4.506	0.775
34.5	1804.3816	-5.796	0.804
36.5	1806.5910	-4.506	0.809
37.5	1807.6957	-4.097	0.810
38.5	1808.8004	-3.854	0.777
39.5	1809.9051	-2.949	0.835
40.5	1811.0098	-2.466	0.834
41.5	1812.1144	-2.277	0.770
42.5	1813.2191	-1.383	0.811
173.5	1957.9329	-2.145	0.897
174.5	1959.0376	-1.105	0.832
175.5	1960.1423	-1.108	0.793
176.5	1961.2470	-3.146	0.809
177.5	1962.3517	-4.163	0.813
178.5	1963.4564	-1.103	0.814
179.5	1964.5610	0.615	0.783
180.5	1965.6657	1.774	0.794
181.5	1966.7704	-1.163	0.793
182.5	1967.8751	-0.928	0.813
184.5	1970.0845	-0.943	0.816
186.5	1972.2938	2.103	0.830
187.5	1973.3985	2.611	0.797
188.5	1974.5032	1.298	0.807
189.5	1975.6079	1.833	0.832
190.5	1976.7126	3.443	0.803
191.5	1977.8173	7.375	0.819
192.5	1978.9220	3.657	0.796
193.5	1980.0266	4.875	0.860
194.5	1981.1313	4.909	0.859

Table A3. O-C values for the secondary eclipses.

Table A4. Photometric observations of TIC 470710327. Data obtained from VizieR (`http://vizier.unistra.fr/vizier/sed/`).

Passband	Effective wavelength [Å]	Flux [erg s^{-1}cm^{-2}Å^{-1}]	Magnitude	Ref.
Johnson:U	3971.00	6.52e-13 ± 3.26e-14	9.38	a
HIP:BT	4203.01	6.40e-13 ± 1.19e-14	9.40	b
HIP:BT	4203.01	6.65e-13 ± 1.53e-14	9.36	c
Johnson:B	4442.03	6.17e-13 ± 1.37e-14	9.44	d
Johnson:B	4442.03	6.47e-13 ± 1.82e-14	9.39	e
SDSS:g'	4819.97	7.88e-13 ± 7.62e-16	9.17	f
HIP:VT	5318.96	5.30e-13 ± 9.54e-15	9.60	b
HIP:VT	5318.96	5.51e-13 ± 1.27e-14	9.56	c
Johnson:V	5537.05	5.48e-13 ± 5.28e-14	9.57	d
Johnson:V	5537.05	4.73e-13 ± 9.78e-15	9.73	f
SDSS:r'	6246.98	4.70e-13 ± 1.54e-14	9.73	f
Gaia:G	6729.95	3.08e-13 ± 4.63e-15	10.19	h
SDSS:i'	7634.91	3.17e-13 ± 7.19e-16	10.16	f
2MASS:J	12390.1	9.94e-14 ± 1.76e-15	11.42	i
Johnson:J	12500.21	9.96e-14 ± 1.92e-15	11.42	j
Johnson:H	16300.16	4.08e-14 ± 1.02e-15	12.39	j
2MASS:H	16494.77	4.02e-14 ± 1.10e-15	12.40	i
2MASS:Ks	21637.85	1.52e-14 ± 2.56e-16	13.46	i
Johnson:K	21900.25	1.46e-14 ± 1.25e-16	13.50	j
WISE:W1	33500.11	2.99e-15 ± 5.34e-17	15.23	k
Johnson:L	34000.10	2.72e-15 ± 5.19e-17	15.33	c
WISE:W2	46000.19	8.56e-16 ± 1.56e-17	16.58	k
Johnson:M	50299.90	6.64e-16 ± 1.18e-17	16.86	c
WISE:W3	115598.23	2.24e-17 ± 6.73e-19	20.54	k
WISE:W4	220906.68	2.98e-18 ± 3.93e-19	22.73	k

Notes. Data from: (a) Reed (2003); (b) Fabricius et al. (2002); (c) Bourges et al. (2017); (d) Ammons et al. (2010); (e) Lasker et al. (2007); (f) Henden et al. (2016); (g) Droege et al. (2007); (h) Altmann et al. (2017); (i) Zacharias et al. (2012); (j) Cutri et al. (2003); (k) Cutri & et al. (2013)